

Evaluating Seismic Hazard Map for Specified Seismic Source Fault Using GIS-based 3D Deterministic Model: a Case Study of Low Seismicity Region in Egypt

Ibrahim DJAMALUDDIN (✉ ibedije@gmail.com)

Hasanuddin University: Universitas Hasanuddin <https://orcid.org/0000-0002-2963-1899>

Poppy Indrayani

Fajar University: Universitas Fajar

Ahmed M. Meneisy

Aswan University

Research Article

Keywords: Earthquake, seismic hazard map, deterministic method, ground motion, spatial model, GIS

Posted Date: February 11th, 2022

DOI: <https://doi.org/10.21203/rs.3.rs-1248750/v1>

License: © ⓘ This work is licensed under a Creative Commons Attribution 4.0 International License.

[Read Full License](#)

1 **Evaluating seismic hazard map for specified seismic**
2 **source fault using GIS-based 3D deterministic model: a**
3 **case study of low seismicity region in Egypt**

4
5 Ibrahim DJAMALUDDIN ^{a, b *}, Poppy INDRAYANI ^c, Ahmed M. MENEISY ^d

6
7 ^aDepartment of Environmental Engineering, Faculty of Engineering, Hasanuddin
8 University, Poros Malino KM 6, Bontomarannu, Gowa Regency 92171, Indonesia
9 Email address: ibedije@gmail.com

10
11 ^bDisaster Risk Reduction Research Center, Faculty of Engineering, Kyushu University,
12 744 Motooka Nishi-ku Fukuoka City 819-0395, Japan
13 Email address: ibrahim@doc.kyushu-u.ac.jp

14
15 ^cGraduate School of Engineering, Fajar University, Prof. Abdurahman Basalamah
16 No.101, Makassar City 90231, Indonesia
17 Email address: poppyindrayani@yahoo.com

18
19 ^dFaculty of Science, Aswan University, Sahary City, Airport Road, Aswan 81528,
20 Egypt
21 Email address: ahmedmeneisy@sci.aswu.edu.eg

22
23
24 *Corresponding author,
25 Ibrahim Djameluddin (Dr., Associate Prof.)
26 Tel: (+62) 8122231975
27 Email address: ibedije@gmail.com

31 **Abstract:**

32 Although Egypt may be considered as an area of low seismicity, it has experienced the
33 recurring destructive effects of earthquakes throughout its history. The damage
34 distribution is significantly affected by fault geometry and the local site effects. Thus, an
35 appropriate assessment of seismic hazard became a major challenge for efficient
36 mitigation of the seismic risk. This study develops the Geographical Information System
37 (GIS) based three-dimensional (3D) deterministic model to evaluate the seismic hazard
38 map for specified seismic source fault for Egypt. The geometry of a fault plane is
39 generated by a fault-modeling algorithm in which multiple 3D plane sets are interpreted
40 by fault trace, geology, and topography. For estimating the local site effects, the study
41 area is modeled by a 3D grid-mesh system and the ground motion propagation is
42 estimated at each grid by considering the spatial analysis of average shear-wave velocity
43 and a soil susceptibility map. The developed model is applied to simulate the seismic
44 hazard maps in particular the October 12, 1992, Dahshour earthquake that caused huge
45 disasters. The simulated seismic hazard maps of the October 12, 1992, Dahshour
46 earthquake are validated at the observation of an isoseismal map and the evidence of the
47 locations that caused serious damages. Furthermore, an evaluation of the expected
48 Dahshour earthquake with magnitude 6.5 and October 11, 1999, Beni Suef earthquake is
49 conducted for seismic risk mitigation study. By utilizing the developed model, our results
50 encourage the GIS approach for seismic hazard analysis where 3D models can lead to a
51 more accurate assessment.

52

53 **Keywords:** Earthquake; seismic hazard map; deterministic method; ground motion;
54 spatial model, GIS

55

56

57

58

59

60

61

62 **1. Introduction**

63 Earthquakes are one of the dangers of natural disasters that can pose risks to human
64 life, loss of property, and environmental damage (Cornell 1968). Tectonic earthquakes
65 occur anywhere on earth where there is sufficient stored energy of elastic strain to
66 promote fracture propagation along the fault plane. The mechanism of destruction occurs
67 because the energy release patterns and shaking effects are propagated to all parts of the
68 earth. On the earth's surface, the shaking can cause damage and collapse of buildings that
69 can cause casualties, and can also trigger landslides, rock collapses, and other soil damage
70 that destroys residential areas. The earthquake also causes secondary disasters in the form
71 of fires, industrial and transportation accidents, and floods due to the collapse of dams
72 and other retaining embankments. In general, earthquakes will damage and destroy
73 densely populated villages with weak building construction, non-earthquake resistant
74 buildings with poor technical design, high-rise buildings built on poor soil conditions,
75 and buildings on unstable slopes (Mohamed et al. 2012).

76 The size of the magnitude scale describes the amount of seismic energy emitted by the
77 earthquake source and the results of seismograph observations. The magnitude of an
78 earthquake with a scale of 3 or less often cannot be felt on the surface or is called weak.
79 The magnitude scale of 7 or greater will potentially cause serious damage in an area.
80 However, earthquake disaster is not dependent only on the magnitude scale but also on
81 the effect of local sites (Abdel-Fattah 1999). Seismic hazard is the probability that an
82 earthquake will occur in a given area and quantification of the seismic ground motion at
83 a specific site. Seismic ground motion level is typically high in the vicinity of the fault
84 plane and decreases with distance from the fault depending on the earthquake magnitude
85 and the geology of the region (Si and Midorikawa 1999). The effect of local sites
86 especially the soft soil layer is the main factor in the intensity of the earthquake shaking
87 because it can amplify the seismic ground motion (Hough et al. 1990; Sabet et al. 2015).
88 For instance, although Egypt may be considered as an area of low seismicity, it has
89 experienced the recurring destructive effects of earthquakes throughout its history
90 (Badawy, 1998). The Dahshour earthquake of October 12, 1992, and the Beni Suef
91 earthquake of October 11, 1999, are well-known examples of a small but affecting
92 earthquake disaster in beneath southwestern Cairo, the northern part of Egypt. Because

93 most of the dense populations, archaeological sites, and vital infrastructures are
94 concentrated around the Nile river valley which is covered by sedimentary soil layers,
95 and the majority of buildings are not yet designed to resist earthquakes; therefore, even
96 relatively small ground motion can be the source of huge disasters. Several earthquake
97 events in the world have occurred in the past, such as the earthquakes in Michoacan,
98 Mexico in 1985 Loma Prieta, California, the USA in 1989, Kocaeli and Düzce, Turkey
99 in 1999, Chi-Chi, Taiwan in 1999, and Wenchuan, China in 2008, reminds us of the
100 significant disasters influenced by the effect of local sites (Borja-Navarrette et al. 1986;
101 Hough et al. 1990; Rathje et al. 2003, 2005; Wen et al. 2010). Hence, an appropriate
102 assessment of the seismic hazard map is a critical element in the earthquake risk
103 management process for Egypt.

104 In recent years, many studies have been carried out on the calculation of seismic
105 ground motions by the application of models (e.g., Boore 1983, 1996, 2003, Ambraseys
106 1995; Joshi et al. 2007; McGuire 1995, 2008; Mustafa and Takenaka 2009; Khaled et al
107 2013; Ordaz et al. 2014). The calculation models can be classified mainly into two
108 approaches. A deterministic calculation approach is applied from a given specified set of
109 seismological parameters, including the determination of specified fault as an earthquake
110 source and distance from the fault to the points at the ground surface for calculating the
111 seismic hazard by attenuation relationships. The probabilistic calculation approach is
112 used to estimate statistically seismic hazards using all possible earthquake sites,
113 magnitudes, and expected probabilities of occurrence. In low seismicity regions for
114 example in the northern part of Egypt, the assessment of seismic hazard using a
115 probabilistic calculation approach must cope with difficult identification of active seismic
116 faults with the low amount of seismic data or some regions without seismic records are
117 available (Badawy 2005). The deterministic calculation approach has important
118 implications for effective earthquake risk management in southwestern Cairo such as El
119 Faiyum, Girza, and Beni Suef areas. Appropriate calculations of the seismic ground
120 motion are required to reliably determine a seismic hazard map. Nevertheless, seismic
121 hazard assessment using a deterministic calculation approach is not an easy and time-
122 consuming task (McGuire 1995; Joshi et al. 2007). The focus is generally on determining
123 the specified seismic source fault at the site through the mapping of the fault rupture plane
124 (i.e. fault length, fault dip, fault depth), the estimation of the ground motion propagation

125 from geological and soil conditions, and the utilization of the ground motion attenuation
126 relationships to simulate the distribution of seismic hazard.

127 It is essential to compute a deterministic seismic hazard map in three-dimensional (3D)
128 model parameters and to provide automation, intellection, and visualization in the
129 scenario-based simulations for Egypt. Moreover, the spatial quantification of the various
130 ground effects at a specific site is an important analysis of the ground motion propagation
131 for a study area. The recent development of Geographical Information Systems (GIS)
132 comprises a technology designed to support integrative modeling and to conduct
133 interactive spatial analysis for understanding various 3D processes (Fortheringham and
134 Wegener 2000). In the present study, a deterministic calculation model using GIS that
135 realistically computes the seismic hazard map for specified seismic source fault is
136 established to obtain a reliable evaluation of seismic risk for Egypt. A fault modeling
137 algorithm in GIS is developed for generating a 3D fault geometry interpreted by fault
138 trace, topography, and geology. A grid-mesh system in GIS is utilized as a 3D model
139 parameter to estimate the ground motion propagation in the study area by considering the
140 spatial analysis of average shear-wave velocity and the soil susceptibility map. For a
141 preliminary assessment, the ground motion attenuation relationships by Si and
142 Midorikawa (1999) are adopted to establish the 3D seismic calculation modeling
143 algorithm using GIS functions for evaluating several scenario earthquakes in the study
144 area. The developed model is applied to evaluate the seismic hazard maps for the
145 Dahshour earthquake and Beni Suef earthquake based on a scenario study.

146

147 **2. Seismic Source Faults in Egypt**

148 **2.1 Historical earthquake sites**

149 The study area (**Fig. 1**) is located in the northern part of Egypt as a part of the Nile
150 river valley, which covers southwestern Cairo including the El-Faiyum, Girza, and Beni
151 Suef areas. According to Badawy and Horvath (1999a, 1999b), most of the earthquake
152 events mainly occur in the northern part of Egypt and are related to the plate boundaries.
153 The relative motion of the Sinai sub-plate concerning the Suez rift and to the Aqaba-Dead
154 Sea rift characterizes the major source of seismic activities in the northern part of Egypt.
155 A relatively low rate of historical earthquake activity also continues on-trend to the

156 southwest Beni Suef area. **Fig. 2** represents the study area remarked by dotted lines and
157 selected historical earthquakes from 1990 to 2018 beneath southwestern Cairo that has
158 been the important site of several earthquake events, in particular, a magnitude 5.9
159 Dahshour earthquake struck about 40km southwestern Cairo on October 12, 1992, caused
160 tremendous damage.

161 **2.2 Geological and tectonic setting**

162 Geology of the study area has been investigated by a variety of authors (e.g. Hume
163 1911; Said 1962; Said and Martin 1964). The study area is mostly covered by sedimentary
164 rocks of different formations belonging to the middle Eocene up to the Quaternary.
165 Generally, the geological formations are composed of Mokattam Group, Wadi Rayan
166 Formation, and shallow marine limestone (Sabet et al. 2015). In the Nile river valley,
167 sediment formations are classified into three types: the Protonile consists mainly of gravel,
168 the Prenile consists of fluvial sand, and the Nile silt consists of fine clastic sediments.
169 According to the Egyptian Geological Survey and Mining Authority (EGSMA) in 1981,
170 Egypt was subjected to several stages since the Precambrian. The Precambrian is
171 characterized by the development of three main fault directions, North-South (N-S),
172 North Northwest-South Southeast (NNW-SSE), and Northeast- Southwest (NE-SW). In
173 the Paleozoic, a new East-West (E-W) trend developed and continued to affect the
174 Mesozoic. The Mesozoic folding structures known in the northern part of Egypt were also
175 affected by a new fault trend in East-Northeast (ENE) and West-Northwest (WNW)
176 directions. The Red Sea became effective in the Northwest- Southeast (NW-SE) and NE-
177 SW trends. **Fig. 3** shows a simplified geologic map from Egyptian General Petroleum
178 Corporation (EGPC) which depicts the different rock formations in the vicinity of the
179 Nile river valley, and the relief map describes the major trend of lineaments. Rose
180 diagram (see **Fig. 3**) reveals that the dominant trend of lineaments tends to run NW-SE
181 and NE-SW. These lineament trends are in correspondence with the previously obtained
182 trends by Badawy and Horvath in 1999.

183 **2.3 A 3D fault modeling algorithm in GIS**

184 The most simplistic method for 3D fault modeling is a simple flat plane. By setting a
185 dip and azimuth the inferred fault can be created. However, if the case involves multiple
186 faults that intersect or consist of multiple parts of a fault plane, manual fault mapping is
187 labor-intensive and time-consuming to determine 3D models (Admasu et al. 2006). In

188 this study, automatic fault mapping is accomplished by using multiple spatial datasets
189 interpreted by fault trace, geology, and topography.

190 **Fig. 4** shows the simplified algorithm of fault modeling using GIS functions that
191 represent several spatial analyses and data manipulation to create the 3D fault model. At
192 the first stage, the spatial analysis and data manipulation are conducted to obtain the
193 multiple datasets of surface z-values interpreted by fault traces and ground surface
194 contour data by Digital Elevation Model (DEM). Subsequent fault calculating fits a
195 surface contour to the highlighted fault dip through the spatial analysis from the
196 geological data. Azimuth Line Points are calculated using the Near Analysis in GIS by
197 interpreting the surface contour and fault trace-points to obtain the calculation of azimuth
198 angles. Azimuth angles at each trace-point are central parameters to estimate the fault
199 shape through a spatial calculation using a mathematical formulation. The second stage
200 of the calculation is conducted to estimate the multiple datasets at irregularly spaced
201 locations by the Dip Line Points. Fault surface searches for a connected, smooth curve
202 with fits the subsurface dataset. This result is then projected to the next inline, providing
203 fault planes. In this stage, the Dip Line Points generates two sets of data points on one
204 side of the ground surface and the other side of the subsurface. Thus, a smooth surface
205 between the two sets of data points is computed by the Triangular Irregular Network
206 (TIN) Analysis. Moreover, the Point Inter-Line is calculated from the Azimuth Line
207 Points that uses to select the calculated orientation of each triangular face of a 3D TIN
208 polygon (fault plane) for example, N-E dip or S-W dip. Finally, fault plane results on a
209 series of successive dataset sections, constitute a 3D fault model by the format of 3D
210 polygon shapefile in the GIS dataset.

211 In the computational implementation system, the 3D fault modeling is accomplished
212 by the use of GIS geoprocessing tools. **Fig. 5a** shows the actual stages of the schematic
213 flow model of geoprocessing tools that comprises a 110-step process to provide an
214 automatic computation of 3D faults for speeding up interpretation on large 3D datasets.
215 The developed schematic flow model is represented as a diagram that chains together
216 sequences of processes using the output of one process as the input to another process.
217 Accordingly, an adjustment model for 3D fault planes can be performed by only changing
218 the input parameters without going through a long-stage process. **Fig. 5b** shows the 3D
219 view of a 3D fault modeling resulting from the selected fault traces (lineaments) beneath

220 southwestern Cairo, the northern part of Egypt, as an example of the result from GIS
221 geoprocessing tools.

222

223 **3. Ground motion propagation**

224 **3.1 Ground motion records in the study area**

225 Observed areas of building damage in southwestern Cairo resulting from October 12,
226 1992, Dahshour earthquake might be related to the ground motion propagation within the
227 Nile river valley which is covered by sedimentary soil layers (Ahmed et al. 1993).
228 However, the opportunity to capture recorded ground motion data from the earthquakes
229 in the northern part of Egypt was lost primarily because of the lack of strong motion
230 instrumentation, inadequate geographic coverage of instrumentation networks presently
231 installed, and inadequate dynamic range of the seismographic instrumentation in place
232 (Thenhaus et al. 1993). Lacking the ground motion records, there is always the question
233 of whether anomalously located areas of damage are due to deficient construction
234 practices or an actual physical enhancement of ground motion propagation.

235 **3.2 A 3D grid-mesh system for site amplification factor**

236 It has been recognized by researchers that soft and young sediments covering firm
237 bedrock can amplify seismic ground motions and cause severe damages during an
238 earthquake event. The shear-wave velocity of shallow sediments is very important in
239 ground motion propagation. Anderson et al. (1986) noted that the strata in the top 30
240 meters have a considerable influence on the character of the created seismic ground
241 motions. The average shear-wave velocity from the surface to 30-meter depth (AVS or
242 Vs30) is a well-known parameter for estimating the site amplification factor (ARV).
243 Table 1 shows the definition in terms of AVS and simple geological descriptions by the
244 National Earthquake Hazard Reduction Program (NEHRP). The ARV between surface
245 and firm bedrock has the following relationship with AVS, described as Eqn. 1.
246 (Midorikawa 1994)

$$247 \log ARV = 1.83 - 0.66 \log AVS, \text{ for } (100 < AVS < 1500) \quad (1)$$

248 where,

249 ARV: the site amplification factor for peak ground velocity (m/s)

250 AVS: the average shear-wave velocity from surface to 30m depth (m/s)

251 In this study, the AVS dataset from the United States Geological Survey (USGS) is
252 used to obtain the AVS contours interpolated from grid points at a 5-kilometer scale as a
253 proxy for the spatial analysis of the site amplification factor. Since the AVS values should
254 be used at finer scales for the study area, the soil susceptibility map by 1:50,000 scale and
255 the interpolated AVS contour map are utilized further by spatial correlation analysis to
256 estimate the AVS at a 50-meter grid scale. This soil susceptibility map is generally based
257 on the distribution of shallow soil profiles over rock beneath the Nile river valley. **Fig. 6**
258 shows the estimated ARV map of the study area that lower shear wave velocities (200 to
259 250 m/s) correspond quite well with the outcrop of unconsolidated Quaternary sediments
260 along the Nile river valley (see **Fig. 3**). The areas consist of soft-stiff sediments like Nile
261 silts that are more susceptible to amplification.

262 In the GIS calculation model, the 3D grid-mesh system (see **Fig.5b**) is used for seismic
263 hazard simulations that will define the accuracy and resolution of the simulation results,
264 both of which will affect the GIS computation time and level of detail in the results of the
265 seismic hazard map. Therefore, it's important to have a site amplification factor that is
266 linked in the 3D grid-mesh for computational simulation. Grid-mesh involves the ground
267 elevation and a site amplification factor to represent the arrangement and spacing between
268 each grid point. The study area which varies in elevation across different mountain ranges
269 or complex surface geological boundaries may require high meshing density to ensure
270 accuracy, which increases the computation time in the simulation. In this study, a
271 rectangular grid by 50-meter is designed to represent the study area for use in a seismic
272 hazard simulation. The result of the estimated ARV map and DEM map are interpolated
273 for the entire simulation domain which has 5,548,164 of the total grids.

274

275 **4. Hazard assessment method**

276 **4.1 Ground motion attenuation relationships**

277 To calculate the seismic hazard for specified seismic source fault in 3D model
278 parameters, the attenuation relationships defined by Si and Midorikawa (1999) are
279 utilized as a preliminary assessment model. The methodology of attenuation relationships
280 used are described as follows:

281 a) Peak ground acceleration (PGA)

282 Peak ground acceleration (PGA) is equivalent to the maximum ground acceleration
 283 that occurred during earthquake shaking at a specific site. The PGA is calculated by the
 284 distance attenuation formula of peak acceleration with shear wave velocity ($V_s = 400$
 285 m/s), described as Eqn. 2.

$$286 \log \text{PGA} = 0.50 M_m + 0.0043 D + d + 0.61 - \log (X + 0.0055 \times 10^{0.5M_m}) - 0.003 X \quad (2)$$

287 where,

288 PGA: peak ground acceleration (cm/s^2 or gal)

289 M_m : moment magnitude

290 X: shortest distance from fault (km)

291 D: hypocenter depth (km)

292 d: fault types

293 b) Peak ground velocity (PGV)

294 Peak ground velocity (PGV) is the maximum respective amplitudes of velocity at the
 295 ground surface. The attenuation relation of peak velocity on the bedrock with shear wave
 296 velocity ($V_s = 600$ m/s) is given as Eqn. 3. By multiplying Eqn. 1 and Eqn. 3, the PGV
 297 at the ground surface is described, as Eqn. 4.

$$298 \log \text{PGV}_{b600} = 0.58 M_m + 0.0038 D + d - 1.29 - \log (X + 0.0028 \times 10^{0.5M_m}) - 0.002 X \quad (3)$$

$$299 \text{PGV} = \text{ARV} \times \text{PGV}_{b600} \quad (4)$$

300 where,

301 PGV_{b600} : peak velocity on the bedrock with average shear wave velocity (600m/s)

302 PGV: peak velocity at the ground surface (cm/s)

303 c) Seismic intensity (SI)

304 Seismic intensity (SI) is calculated using the relation between the intensity and the
 305 peak ground velocity, described as Eqn. 5.

$$306 \text{SI} = 2.68 + 1.72 \log \text{PGV}, \text{ for } (4 \leq I \leq 7) \quad (5)$$

307 where,

308 SI: seismic intensity

309 **4.2 3D calculation modeling algorithm in GIS**

310 There are two spatial datasets of the input parameter for conducting a computational
 311 process of the seismic hazard assessment within GIS. The first dataset is 3D polygons as
 312 a fault geometry model, and the second dataset is a 3D grid-mesh system as a ground
 313 motion propagation model. Other parameters such as earthquake magnitudes, hypocenter

314 depth, fault types, etc. are specified in the 3D polygon dataset. The 3D seismic hazard
315 calculations are performed within GIS. The function of GIS is used as a spatial-temporal
316 database for extracting, calculating, and updating the input data.

317 **Fig. 7** shows the algorithms of the 3D seismic hazard calculation model for specified
318 seismic source fault. By the functions of GIS, the operator interface of point collection
319 (IPointCollection) read the input of the 3D polygon of fault model in the computational
320 system of GIS to access and manipulate the Polygons. IPointCollection can be used to
321 create Multipoints from polygon vertices in 3D return references to the points in the
322 collection. Multipoints containing x , y , and z values are used to calculate the fault plane
323 equation of a polygon. Assume that a polygon is given by its vertices $v1, v2, \dots, vn$, in
324 cycle order, and each vi is given by its coordinates in 3D: $vi = (xi, yi, zi)$. The fault plane
325 equation, $Ax + By + Cz + D = 0$ is given by the equation of vectors. By computing the
326 fault plane equation of a polygon, A , B , C , and D can be obtained. New coordinates for
327 each polygon vertex and plane angles can be computed by using the formula and operator
328 interface to provide the coordinate conversion process from global to the local projected
329 system in GIS. Operator interface of geometry (IGeometry) and proximity
330 (IProximityOperator) is applied to define the sides of the polygon and the projected
331 polygon and to compute the distances (L_f) from points to points in the polygon,
332 sequentially. IProximityOperator is also used to calculate the nearest points from the grid-
333 mesh system as ground motion calculation points (ground surface points) to the projected
334 polygon points. The formula of the calculation of real distance is established to compute
335 the real height distance (L_h) from the calculated fault point to the ground surface. To
336 obtain the shortest distance (L_s) from a surface point to the 3D polygon (fault plane), nine
337 cases of the mathematical algorithm are developed which depend on the position of fault
338 sides to the calculation points and the parameters of L_f and L_h . Generally, the shortest
339 distance (L_s) from (x_0, y_0, z_0) to the 3D polygon plane $Ax + By + Cz + D = 0$ is given by
340 following formula.

$$341 \quad L_s = \frac{|Ax_0 + By_0 + Cz_0 + D|}{\sqrt{A^2 + B^2 + C^2}} \quad (6)$$

342 Accordingly, a GIS-based computational model arrays the result of shortest distance
343 values for all the point coordinate at the designed 3D grid-mesh system for each 3D
344 polygon, and calculates the seismic hazard based on the earthquake parameters (**Fig. 8**).

345 **5. Hazard assessment case studies**

346 There are three scenarios for the seismic hazard simulation in the study area. Case 1 is
347 to validate October 12, 1992, Dahshour earthquake with magnitude 5.9. The 3D fault
348 model used in the present study is derived from the 1992 Dahshour mainshock, estimated
349 by Hussein et al. (1996) with specific parameters (depth of epicenter is 22 km, fault depth
350 to the upper edge is 12 km, length of fault is 12 km, width of fault is 10 km), and main
351 fault orientation is 270° (strike) and 47° (dip). Case 2 is to assess the maximum expected
352 Dahshour earthquake with a magnitude of 6.5. Case 3 is to evaluate October 11, 1999,
353 Beni Suef earthquake with magnitude 4.9. The 3D fault model is interpreted with specific
354 parameters (depth of epicenter is 26 km, fault depth to the upper edge is 15 km, length of
355 fault is 5 km, width of fault is 12 km), and main fault orientation is 153° (strike) and 72°
356 (dip) (Abou-Elenean and Deif 2003).

357

358 **6. Results and Discussion**

359 A similar study of October 12, 1999, Dahshour earthquake has been conducted by
360 several researchers (Hussein et al. 1996; Hussein 1999; Hussein and Farouk 2000; Abou
361 Elenean et al. 2000; Moustafa and Takenaka 2009; Khaled et al. 2013). The stochastic
362 approach is mostly used to calculate the peak ground acceleration (PGA). The rectangle
363 fault plane is subdivided into an appropriate number of sub-faults which are modeled as
364 point sources, and the site amplification factor is not yet considered in the seismic hazard
365 map for Egypt. In this study, seismic hazard simulations have taken several procedures,
366 which range from the development of various kinds of spatial datasets that permit the
367 interpretation of the specified earthquake fault sources in 3D, the estimation of the local
368 site effects including soil and topography to input in the 3D grid-mesh system, and the
369 3D calculation of the shortest distance by the attenuation relationships for simulation
370 accuracy. Seismic hazard simulations including the peak ground velocity calculation and
371 seismic intensity calculation were established to evaluate the detailed distribution areas
372 for each hazard level in the study area. The simulation of seismic hazard maps for the
373 Dahshour earthquake and Beni Suef earthquake were performed that assume scenarios
374 for the rupture of a seismic source fault by previous studies. Although there is a lack of
375 validation studies in the region, the 3D input parameters used for the seismic hazard maps

376 are fruitful to be based for reliable disaster risk reduction in the region. The detailed
377 results of the seismic hazard maps are described in two following sections.

378 **6.1 The Dahshour earthquake**

379 The first step of analysis includes the validation of the simulation model of the October
380 12, 1999, Dahshour earthquake at the observation of isoseismal map according to the
381 MMI scales, as currently available data. **Fig. 9** shows the location of the designed
382 simulation region for evaluating seismic hazard maps as a study area marked by a red
383 dotted line that overlaid with the isoseismal map of the MMI observation of October 12,
384 1992, Dahshour earthquake, established by Thenhaus et al. in 1993. The isoseismal map
385 represents the contours of the highest predominant MMI levels about the observed
386 building damages on the west side of the Nile river valley including the areas of El-
387 Faiyum, Girza, and Beni Suef, in the study area. According to Thenhaus et al. (1993), the
388 earthquake on October 12, 1992, occurred in Dahshour with the highest of the MMI level
389 (MMI = VIII) that caused tremendous damage performing major disaster in the Nile river
390 valley. The observed soil liquefaction near the earthquake epicenter (MMI = VIII)
391 occurred in the alluvial Nile deposits at many sites near the Barnasht to El Aiyat Districts
392 (Japanese Expert Team 1993; Ahmed et al. 1993). On the isoseismal map, the seismic
393 intensity distributions ranging from level VI to level VII are mostly located in Cairo, El
394 Faiyum, Girza, and also Beni Suef. Serious building damage areas were investigated in
395 Cairo, El-Faiyum, and Girza. On contrary, no building and infrastructure damage was
396 observed in the Beni Suef area. **Fig. 10a** shows the simulation result for peak ground
397 velocity. The distribution of the maximum respective amplitudes of velocity at the ground
398 surface that exhibits some low (dark green to green colored) and moderate (light green to
399 yellow colored) values, and reveals a prominent very strong level (MMI = VII-VIII) as
400 major damage areas, located in the front area of the rupture propagation of the Dahshour
401 fault. Table 2 shows the statistical result of surface velocity distribution at each MMI
402 level. The ranges of the observed MMI are compared by the simulated model. Moreover,
403 **Fig. 10b** shows the simulation result of the distribution of the seismic intensity map
404 overlaid by the smoothed contours (dotted lines) from the isoseismal map representing
405 the highest predominant intensity levels of MMI. The overall concentration and
406 distribution of seismic intensity calculated are mostly consistent with the MMI
407 distribution levels. The largest misfit is observed in the low-intensity range (MMI V).

408 However, it is sometimes difficult to identify whether the reason for the misfit of each
409 intensity range is site amplification or attenuation relationships. Taking into account the
410 seismic hazard maps of the October 12, 1992, Dahshour earthquake, the overall
411 agreement between the simulated and observed is satisfactory according to the seismic
412 hazard distributions and the locations of the observed serious damage areas. The
413 simulated model indicates the detailed distribution of seismic hazard levels than the
414 observed MMI contours. For example, the distribution of low hazard levels in the Beni
415 Suef area can be identified more precisely.

416 Moreover, **Fig. 11a-b** shows the simulation results of a scenario study of seismic
417 hazard maps by a maximum expected magnitude 6.5 Dahshour earthquake. The seismic
418 hazard areas beneath southwestern Cairo are greatly increased by about more than double
419 that indicated by the detailed distribution of peak ground velocity and seismic intensity
420 levels. Predictably, the effects could be much worse in Cairo, Girza, and El Faiyum than
421 those experienced in the 1992 Dahshour earthquake. In addition, the potential for
422 widespread liquefaction is very high on the Nile floodplain near the village of Manshiyat-
423 Fadil. Accordingly, the disaster risk mitigation in the northern part of Egypt should be
424 measured by maximum expected seismic hazard maps that are valuable to evaluate the
425 earthquake-resistant design of structural buildings as well as land-use planning in the
426 future. The developed seismic hazard map can estimate the potential damages in the study
427 area that needs to be investigated further.

428 **6.2 The Beni Suef earthquake**

429 The first event of October 11, 1999, the Beni Suef earthquake was the largest observed
430 earthquake to occur in the Beni Suef area. The maximum observed intensity of MMI
431 levels was VI at the epicenter and IV at the Beni Suef area (Abou-Elenean and Deif 2003).
432 **Fig. 12a-b** shows the simulation of the distribution of the surface velocity and seismic
433 intensity for the October 11, 1999, Beni Suef earthquake. Relatively high seismic
434 intensity near the fault and along the Nile river valley is identified because of strong
435 motions raised from spatial distance factors to site amplification. According to
436 Midorikawa (2006), large ground motion variations near faults for inland crust
437 earthquakes are caused by fault propagation effects or the heterogeneous distribution of
438 asperities. The higher values of the seismic intensity are mostly observed along the Nile
439 River covered by alluvial lowland zones. This seismic hazard map allows the

440 identification of the detailed distribution of hazard levels affecting a given site in the Beni
441 Suef area. The simulation result shows that the Beni Suef area lies at a relatively high
442 hazard because of the increased ground motion propagation. Consequently, the site
443 amplification requires detailed investigations of each geologic setting. Although there is
444 a lack of relevant studies in the study area, the developed seismic hazard maps can be
445 used for evaluating seismic risk from future earthquakes in the region. The results of this
446 study describe that the GIS-based 3D calculation model is useful to simulate the
447 distributed hazard levels for the Beni Suef earthquake. For more suitable assessment,
448 detailed site-specific amplification and attenuation relationship studies are very important.
449

450 **7. Conclusion**

451 The evaluation of seismic hazard maps for specified seismic source faults in the
452 northern part of Egypt is conducted in GIS. The fault model is developed using multiple
453 spatial datasets interpreted by fault trace, geology, and topography. A schematic flow of
454 fault modeling using geoprocessing tools are established for automatic computation of
455 numerous spatial analysis and data manipulation to obtain the 3D polygon dataset as the
456 3D fault model parameter. The site amplification factor is estimated from the average
457 shear-wave velocity and soil susceptibility map of the study area through spatial analysis
458 in GIS. Moreover, the 3D grid-mesh system is used as a domain computation for the
459 ground motion propagation model parameter. By implementing the functions of GIS, a
460 3D modeling algorithm using the attenuation relationships is conducted to calculate the
461 seismic hazard for all the points coordinated at the 3D grid-mesh system.

462 The results of this study accomplished the simulation of the seismic hazard of the
463 October 12, 1992, Dahshour earthquake, the scenario study for the maximum expected
464 magnitude 6.5 Dahshour earthquake, and the October 11, 1999, Beni Suef earthquake.
465 The simulation of the 1992 Dahshour earthquake is validated at the observation of the
466 MMI distribution of the isoseismal map and the reliability of the simulated model is
467 verified by comparing the evidence of the observation areas that caused serious damages.
468 The overall agreement between the simulated and observed is satisfactory. Simulation
469 result of October 11, 1999, Beni Suef earthquake also describes that the study area lies at
470 a relatively high hazard because of the increased ground motion propagation in particular

471 along the Nile river valley. Accordingly, the results of the developed seismic hazard map
472 are more effective in evaluating future seismic risk mitigation for Egypt.

473

474

475

476

477

478

479

480

481

482

483

484

485

486

487

488

489

490

491

492

493

494

495

496

497

498 **References**

- 499 1) Abdel-Fattah AK (1999) Source characteristics of the 28th January 1999 Nagano
500 earthquake, Japan. Bull Int Inst Seism Earthq Eng (IISEE) 35:45-57
- 501 2) Abou-Elenean, KM, Hussein HM, Abu El-Ata AS, Ibrahim EM (2000)
502 Seismological aspects of the Cairo earthquake, 12th October 1992, Ann Geofis 43:
503 485-504
- 504 3) Abou-Elenean KM, Deif AG (2003) Seismological Aspects and Source Parameters
505 of Beni Suef Earthquake on 11 October 1999. Bull Fac Sci Cairo Univ. 70:120-142
- 506 4) Admasu F, Back S, Toennies K (2006) Autotracking of faults on 3D seismic data J
507 Geophys 70:49-53
- 508 5) Ahmed WE, Mohamed A, Korhan (1993) A Liquefaction During October 12, 1992,
509 Egyptian Dahshure Earthquake. In Proc of Int Conf on Case Histories in
510 Geotechnical Eng, 14-18
- 511 6) Ambraseys NN (1995) The prediction of earthquake peak ground acceleration in
512 Europe. Earthq Eng Struct Dyn 24:467-490
- 513 7) Anderson JG, Bodin P, Brune NJ, Prince J, Singh SK, Quaas R, Onate M (1986)
514 Strong ground motion from the Michoacan, Mexico Earthquake. Sci 233:1043-
515 1049
- 516 8) Anon. (1987) Egyptian General Petroleum Corporation (EGPC), Geologic map of
517 Egypt
- 518 9) Anon. (1993) Report of Japan disaster relief team on the earthquake in Arab,
519 Republic of Egypt of October 12, 1992. Japan International Corporation Agency
520 (JICA), p 89
- 521 10) Badawy A (1998) Earthquake hazard analysis in northern Egypt. Acta Geod Geoph
522 Hung 33:341-357
- 523 11) Badawy A, Horvath F (1999a) Sinai subplate and kinematic evolution of the
524 northern Red Sea. J Geodynamics 27:433-450
- 525 12) Badawy A, Horvath F (1999b) Seismicity of the Sinai subplate region: Kinematic
526 implications. J Geodynamics 27:451-468
- 527 13) Badawy A (2005) Seismicity of Egypt. Seismol Res Lett 76:149-160

- 528 14) Boore DM (1983) Stochastic simulation of high-frequency ground motions based
529 on seismological models of the radiated spectra. Bull Seismol Soc Am 73:1865-
530 1894
- 531 15) Boore DM (1996) SMSIM - Fortran programs for simulating ground motions from
532 earthquakes: Version 1.0. US Geol Surv Open-file Rep, p 73
- 533 16) Boore DM (2003) Simulation of ground motion using the stochastic method. Pure
534 Appl Geophys 160:635-676
- 535 17) Borja-Navarrette, Diaz-Canales GM, Vera AV, Valle-Calderon ED (1986) Damage
536 statistics of the September 19, 1985, Earthquake in Mexico City. ASCE 70-77
- 537 18) Cornell CA (1968) Engineering seismic risk analysis. Bull Seismol Soc Am
538 58:1583-1606
- 539 19) Fortheringham SA, Wegener M (2000) Spatial models and GIS, new potential and
540 new models. Taylor & Francis, London, 8-10
- 541 20) Hough SE, Borchardt RD, Friberg PA, Busby R, Field EF, Jacob KH (1990)
542 Sediment-induced propagation and the collapse of the Nimitz freeway. Nature
543 344:853-855
- 544 21) Hume WE (1911) The effect of secular oscillation in Egypt during the Cretaceous
545 and Eocene periods. Quart J Geol Soc 67:118-148
- 546 22) Hussein HM, Korrat IM, Abdel-Fattah AK (1996) The October 12, 1992 Cairo
547 earthquake a complex multiple shock. Bull Int Inst Seism Earthq Eng (IISEE) 30:9-
548 21
- 549 23) Hussein HM (1999) Source process of the October 12, 1992 Cairo Earthquake.
550 Annali Di Geofisica 42: p4
- 551 24) Hussein HM, Farouk MA (2000) Spectral analysis and scaling relations of Cairo
552 Earthquake sequence of Oct. 12, 1992 recorded at KEG VBB Station. ICEHM2000,
553 Cairo University, Egypt, 102-117
- 554 25) Joshi A, Mohan K, Patel RC (2007) A deterministic approach for preparation of
555 seismic hazard maps in North East India. Nat Hazards 43:129-146
- 556 26) Khaled O, Mohsen A, El-Sayed F, Awad H, Hussein E (2013) Modeling of strong
557 ground motion during the 1992 Cairo earthquake in the urban area northern Greater
558 of Cairo, Egypt. NRIAG Journal of Astronomy and Geophysics 2:166-174

- 559 27) McGuire R (2008) Probabilistic seismic hazard analysis: Early history. *Earthq Eng*
560 *Struct Dyn* 37:329-338
- 561 28) McGuire RK (1995) Probabilistic seismic hazard analysis and design earthquakes:
562 closing the loop. *Bull Seismol Soc Am* 85:1275-1284
- 563 29) Midorikawa S, Matsuoka M, Sakugawa K (1994) Site effects on strong-motion
564 records observed during the 1987 Chiba-ken Toho-oki Japan earthquake. In *proc of*
565 *9th Japan Earthquake Eng Symp* 3:85-90
- 566 30) Midorikawa S (2006) Some problems related to empirical predictions of strong
567 motion. *Bull Earthq Res Inst Univ Tokyo* 81:253–258
- 568 31) Mohamed AA, El-hadidy M, A. Abou-Elenean KM (2012) Seismic hazard studies
569 in Egypt. *NRIAG J Astron Geophys* 1:119-140
- 570 32) Mustafa Sayed SR and Takenaka H (2009) Stochastic ground motion simulation of
571 the 12 October 1992 Dahshour earthquake. *Acta Geophysica* 57:636-656
- 572 33) Ordaz MG, Cardona OD, Salgado-Gálvez MA, Bernal-Granados GA, Singh SK,
573 Zuloaga-Romero D (2014) Probabilistic seismic hazard assessment at global level.
574 *Int J Disaster Risk Reduct* 10:419-427
- 575 34) Rathje EM, Stokoe IKH, Rosenblad B (2003) Strong motion station
576 characterization and site effects during the 1999 earthquakes in Turkey. *Earthquake*
577 *Spectra* 19:653-675
- 578 35) Rathje EM, Kockar M, Ozbey MC (2005) Observed site effects during the 1999
579 Chi-Chi Earthquake and its aftershocks. *Bull Seismol Soc Am* 76: p 238
- 580 36) Sabet H, Saad A, Abd-Elhamied F (2015) Geotechnical study at 15 May City, Cairo,
581 Egypt. *Int J Innovative Sci Eng Tech* 2(8):960-977
- 582 37) Said R (1962) *The Geology of Egypt*. Amsterdam London, New York, p 377
- 583 38) Said R, Martin L (1964) Cairo area geological excursion notes. In *Proc of Pert Expl*
584 *Soc Liya*, 107-121
- 585 39) Si H, Midorikawa S (1999) Attenuation relations for peak ground acceleration and
586 velocity considering effects of fault type and site condition. *J Struct Construct Eng*
587 523:63-70
- 588 40) Thenhaus PC, Sharp RV, Celebi M, Ibrahim ABK, Van-de-Pol H (1993)
589 Reconnaissance report on the 12 October 1992 Dahshour, Egypt, Earthquake. *US*
590 *Geol Surv Open-file Rep*, 93-181

591 41) Wen RZ, Ren YF, Zhou ZH, Shi DC (2010) Preliminary site classification of free-
592 field strong motion stations based on Wenchuan earthquake records. Earthq Sci
593 23:101-110

594

595

596

597

598

599

600

601

602

603

604

605

606

607

608

609

610

611

612

613

614

615

616

617

618

619

620

621

622 **Statements and Declarations**

623 a) Funding

624 *The authors declare that no funds, grants, or other support were received during the*
625 *preparation of this manuscript.*

626

627 b) Competing Interests

628 *The authors have no relevant financial or non-financial interests to disclose.*

629

630 c) Author Contributions

631 *All authors contributed to the study's conception and design. Material preparation and*
632 *data collection were performed by Ibrahim Djamaluddin and Ahmed M. Meneisy.*
633 *Interpretation of data and analysis were performed by Ibrahim Djamaluddin and Poppy*
634 *Indrayani. The first draft of the manuscript was written by Ibrahim Djamaluddin and all*
635 *authors commented on previous versions of the manuscript. All authors read and*
636 *approved the final manuscript.*

637

638

639

640

641

642

643

644

645

646

647

648

649

650

651

652

653 **Table captions**

654

655 Table 1 NEHRP site definition in terms of Vs30 and simple geological descriptions

656

657 Table 2 Simulated surface velocity at MMI level areas for October 12, 1992, Dahshour
658 earthquake

659

660

661 **Figure captions**

662

663 **Fig. 1** Location map of the study area

664

665 **Fig. 2** Selected earthquakes beneath southwestern Cairo from 1990 to 2018 from the
666 USGS world database of earthquakes

667

668 **Fig. 3** Geological map of the study area (after the Egyptian General Petroleum
669 Corporation, 1987) and colored shaded relief map overlaid the extracted lineaments (solid
670 red lines)

671

672 **Fig. 4** Fault modeling algorithm using GIS functions

673

674 **Fig. 5a** Schematic flow diagram analysis for automatic computation of 3D fault model
675 using GIS geoprocessing tools

676

677 **Fig. 5b** 3D view of the 3D fault modeling result from the selected lineaments covering
678 an area about 100 km² with detailed structural interpretation involves extruding the fault
679 surfaces and fault orientations that overlaid with a 3D grid-mesh system

680

681 **Fig. 6** Estimated ground motion propagation map from the average shear-wave velocity
682 and soil susceptibility map

683

684 **Fig. 7** 3D calculation modeling algorithm using GIS functions to calculate the seismic
685 hazard by the attenuation relationships

686

687 **Fig. 8** Illustration of shortest distance from a 3D surface point (A) to the fault plane (P)

688

689 **Fig. 9** Modified Mercalli Intensity (MMI) distribution map of October 12, 1992,
690 Dahshour earthquake (after Thenhaus et al. 1993), and study area (red dotted lines)

691

692 **Fig. 10a** Simulation of surface velocity distribution map of October 12, 1992, Dahshour
693 earthquake overlaid with the MMI observation contours and the identified seriously
694 damaged areas

695

696 **Fig. 10b** Simulation of seismic intensity distribution map of October 12, 1992, Dahshour
697 earthquake overlaid with the MMI observation contours and the identified seriously
698 damaged areas

699

700 **Fig. 11a** Simulation of surface velocity distribution map of expected 6.5 magnitudes
701 Dahshour earthquake

702

703 **Fig. 11b** Simulation of seismic intensity distribution map of expected 6.5 magnitudes
704 Dahshour earthquake

705

706 **Fig. 12a** Simulation of surface velocity distribution map of October 11, 1999, Beni Suef
707 earthquake

708

709 **Fig. 12b** Simulation of seismic intensity distribution map of October 11, 1999, Beni Suef
710 earthquake

711

712

713

714

715

716 **Tables**

717

718 Table 1 NEHRP site definition in terms of AVS and simple geological descriptions

NEHRP	Description	Range of AVS (m/s)
A	Hard rock	AVS >1500
B	Firm to hard rock	1500 ≥ AVS >760
C	Dense soil and soft rock	760 ≥ AVS > 360
D	Stiff soil	360 ≥ AVS > 180
E	Soft soil	180 ≥ AVS

719

720

721 Table 2 Simulated surface velocity at MMI level areas for October 12, 1992, Dahshour

722 earthquake

Iseismal map			Simulation map			
Scale level	Velocity range (cm/s)	Potential damage	Velocity distribution at each MMI level (cm/s)			
			Average	Min	Max	Sdv
V. Moderate	3.4 – 8.1	Very light	3.31	0.83	6.67	1.10
VI. Strong	8.1 – 16	Light	8.89	3.15	17.93	2.63
VII. Very strong	16 – 31	Moderate	18.16	7.95	30.78	4.69
VIII. Severe	31 – 60	Moderate to heavy	32.71	15.24	52.96	8.79

723

724

725

726

727

728

729

730

731

732

733

734

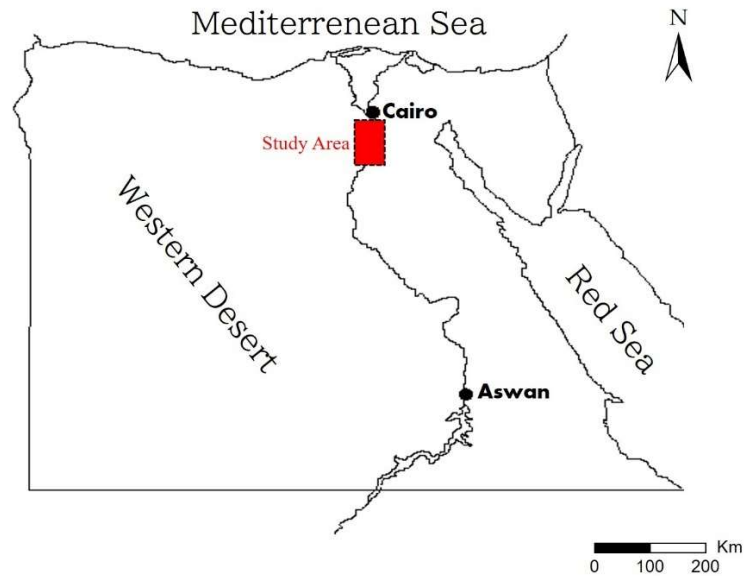
735

736

737

738 **Figures**

739

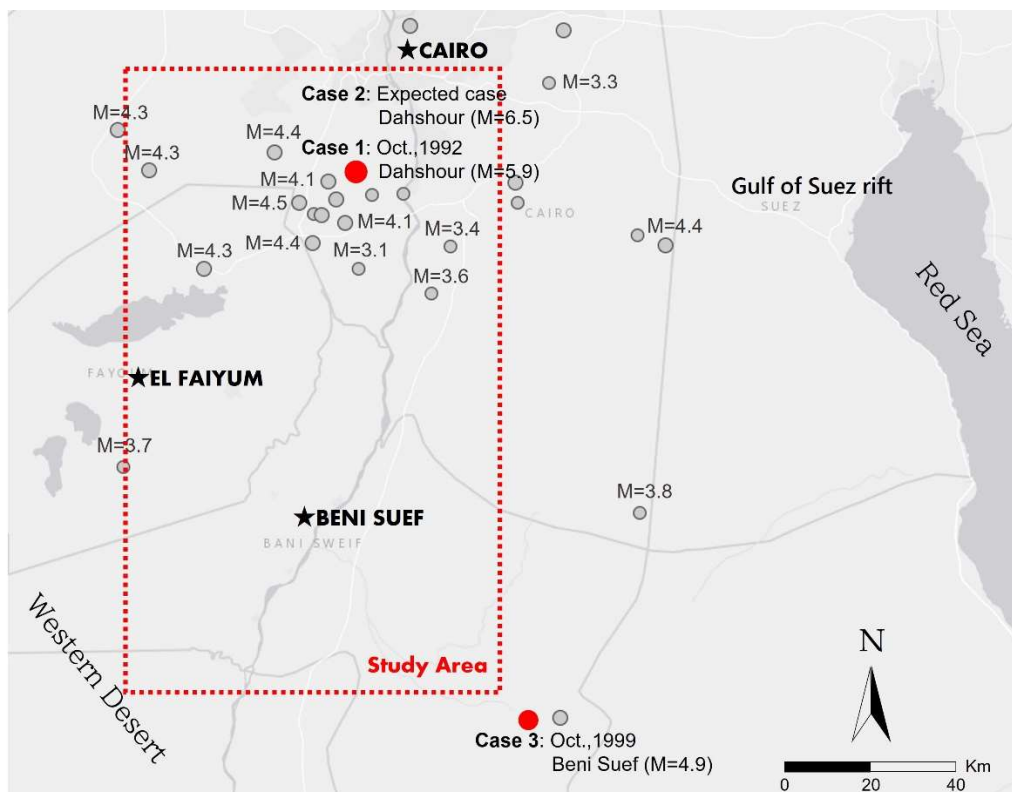


740

741

742

Fig. 1 Location map of the study area

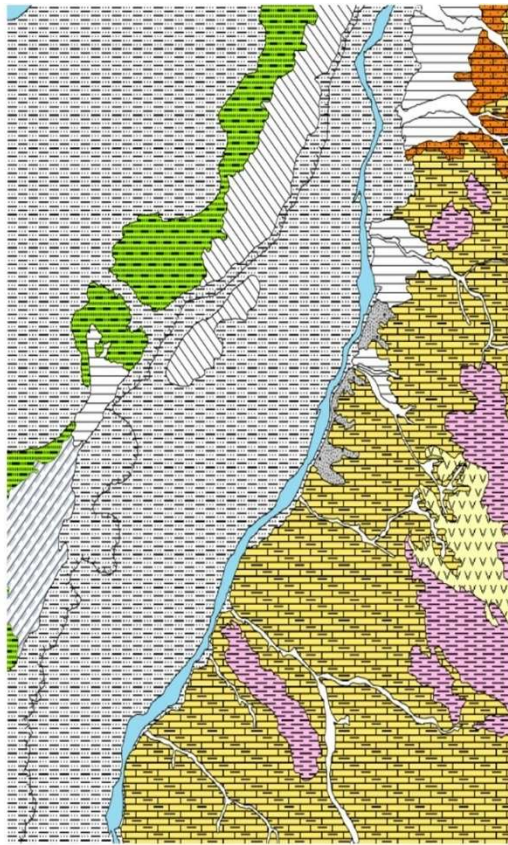


743

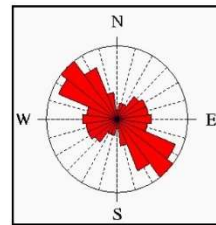
744

745

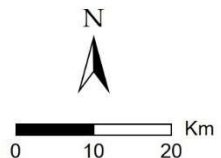
Fig. 2 Selected earthquakes beneath southwestern Cairo from 1990 to 2018 from the USGS world database of earthquakes



Legend



Rose diagram (the lineament trends)



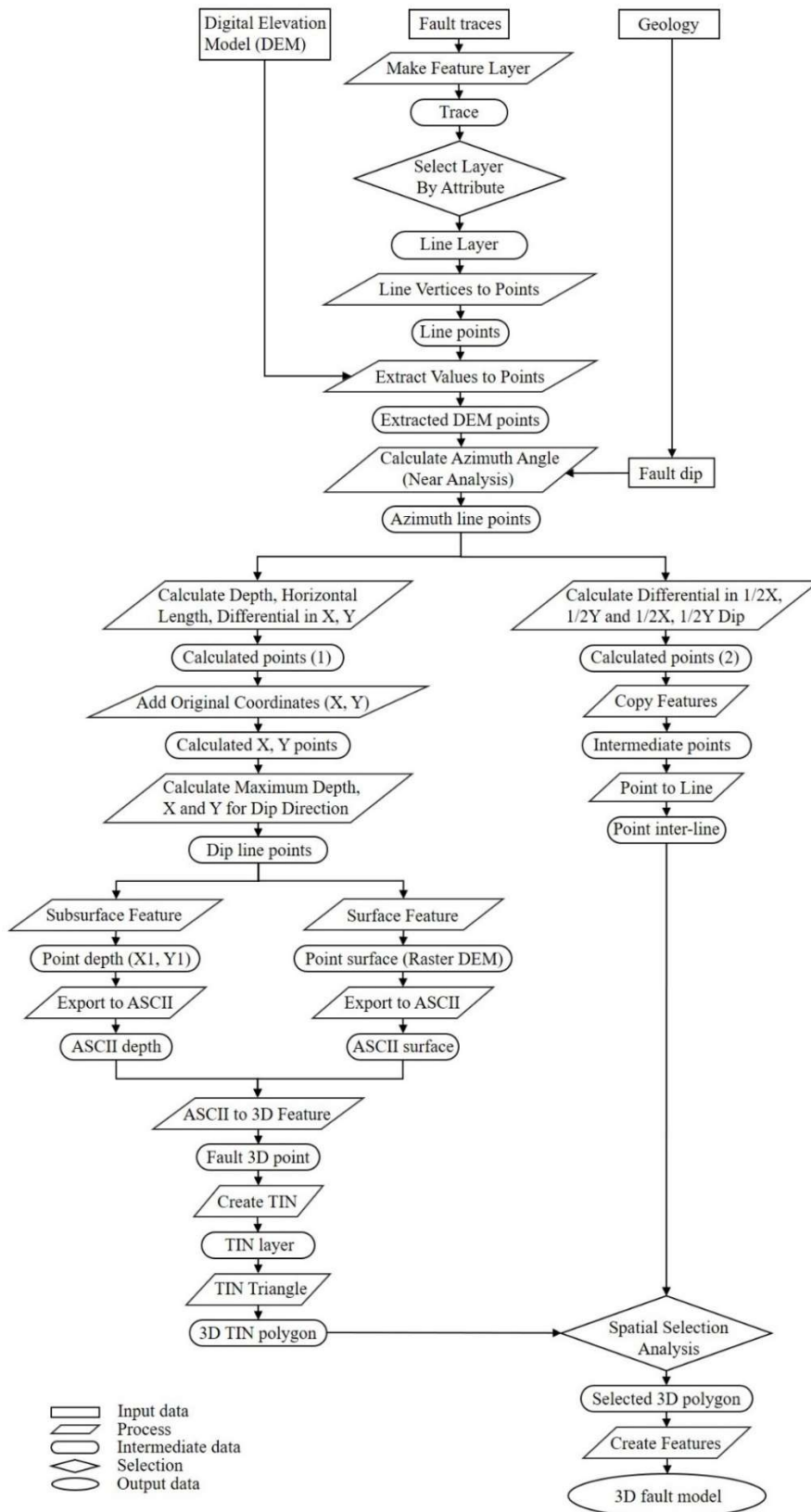
746

747

748

749

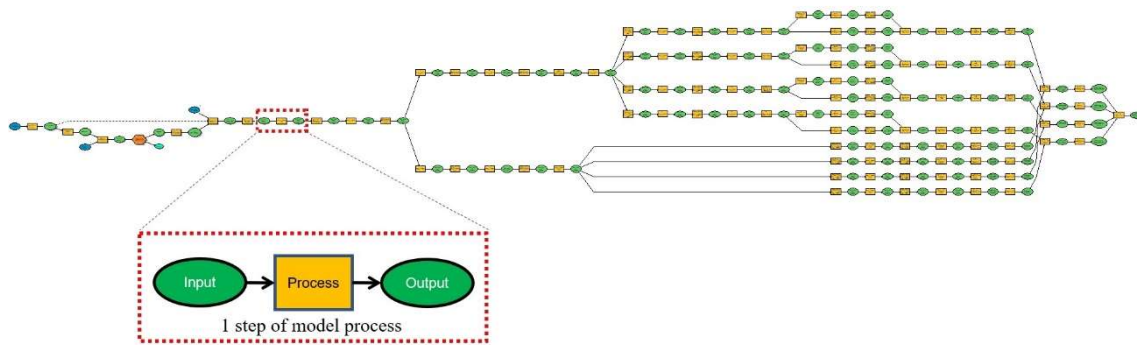
Fig. 3 Geological map of the study area (after the Egyptian General Petroleum Corporation, 1987) and colored shaded relief map overlaid the extracted lineaments (solid red lines)



750

751

Fig. 4 Fault modeling algorithm using GIS functions



752

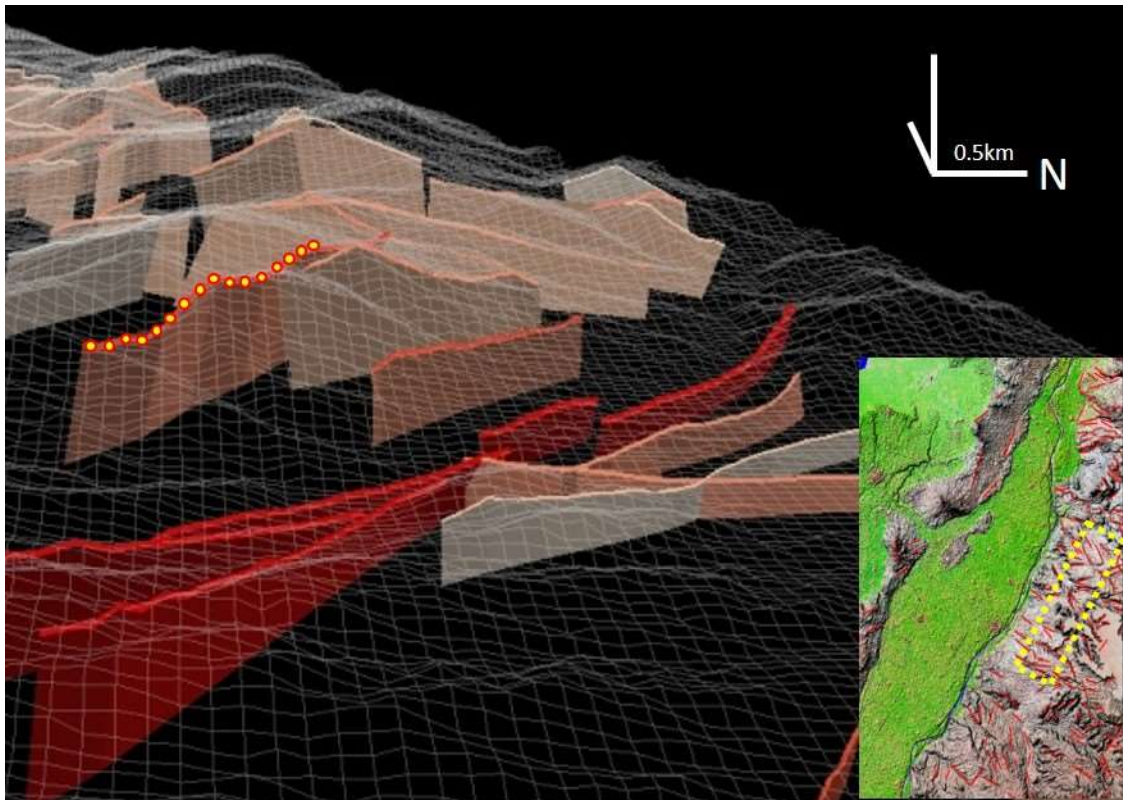
753

Fig. 5a Schematic flow diagram analysis for automatic computation of 3D fault model using GIS geoprocessing tools

754

755

756



757

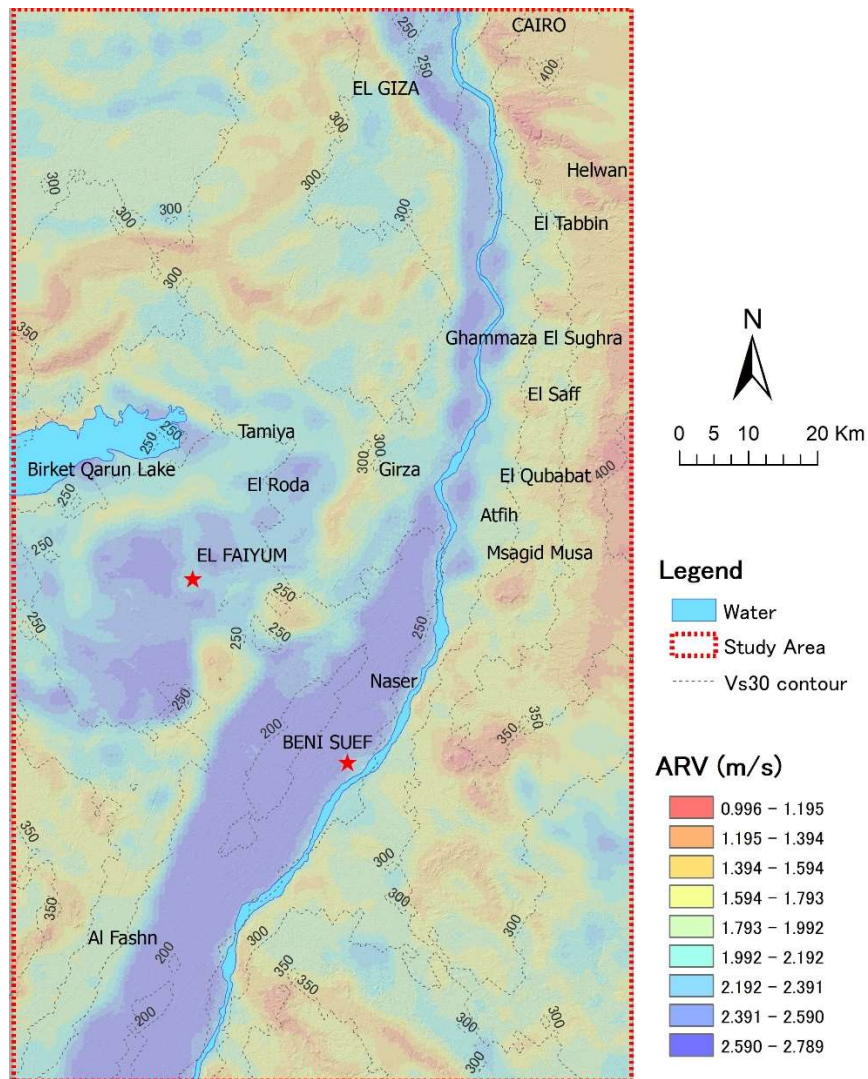
758

Fig. 5b 3D view of the 3D fault modeling result from the selected lineaments covering an area about 100 km² with detailed structural interpretation involves extruding the fault surfaces and fault orientations that overlaid with a 3D grid-mesh system

759

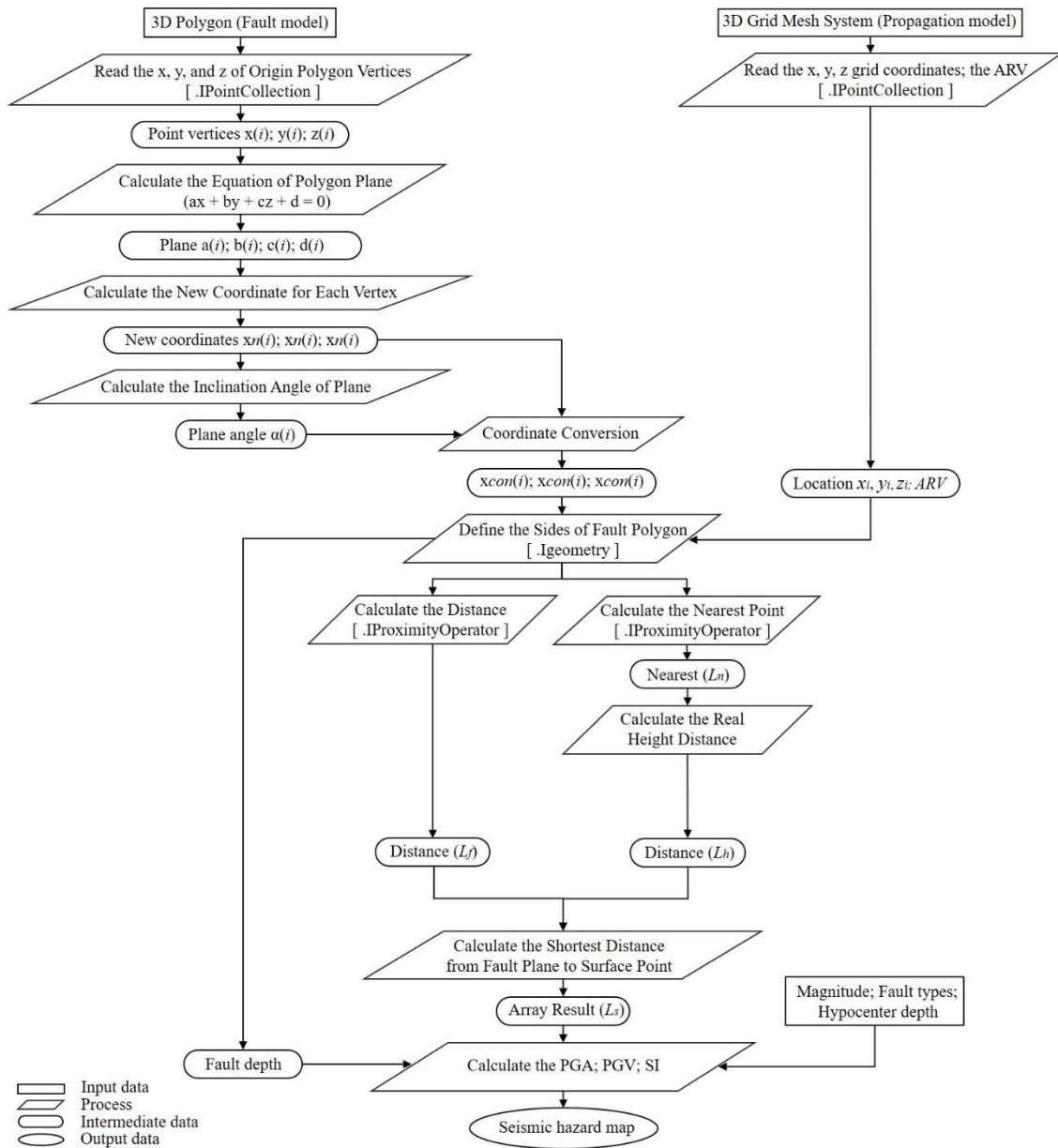
760

761



762
 763
 764
 765
 766
 767
 768

Fig. 6 Estimated ground motion propagation map from the average shear-wave velocity and soil susceptibility map



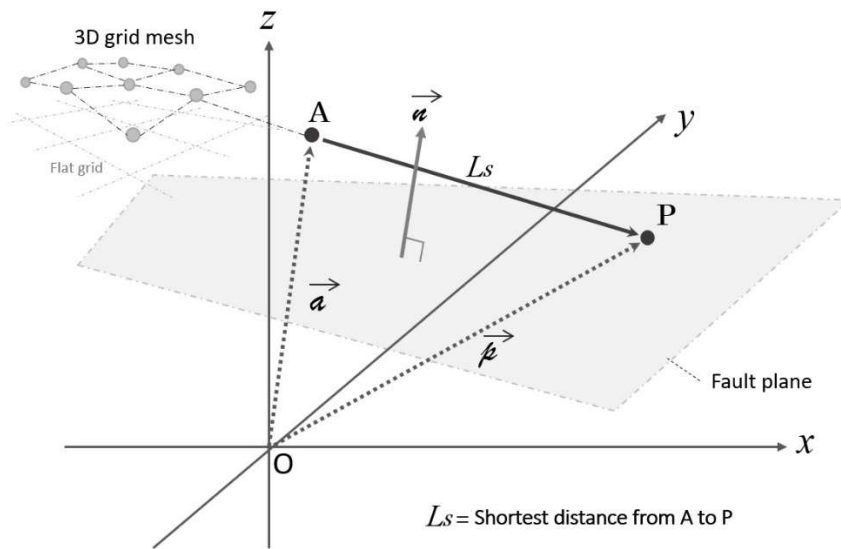
769

770

Fig. 7 3D calculation modeling algorithm using GIS functions to calculate the seismic hazard by the attenuation relationships

771

772

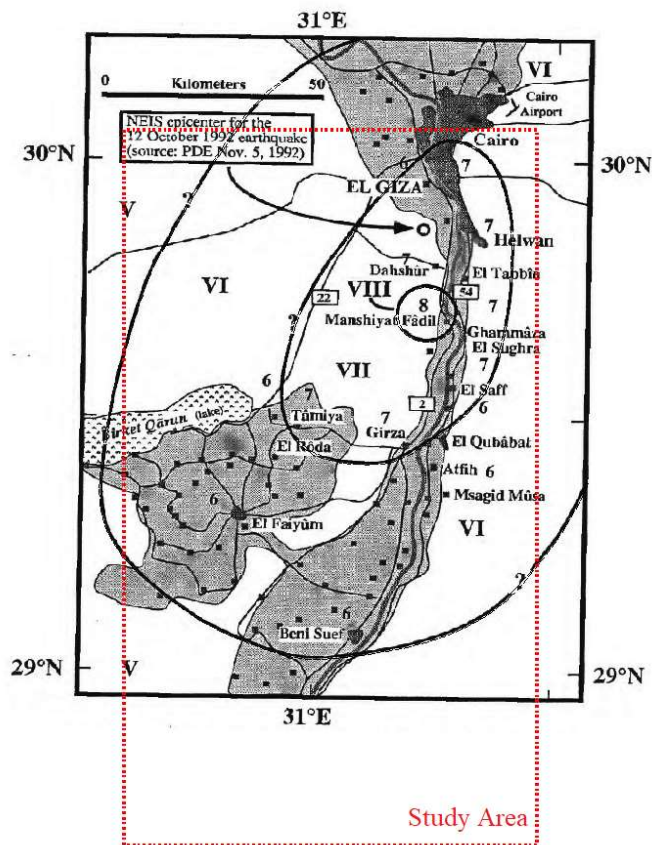


773

774

Fig. 8 Illustration of shortest distance from a 3D surface point (A) to the fault plane (P)

775

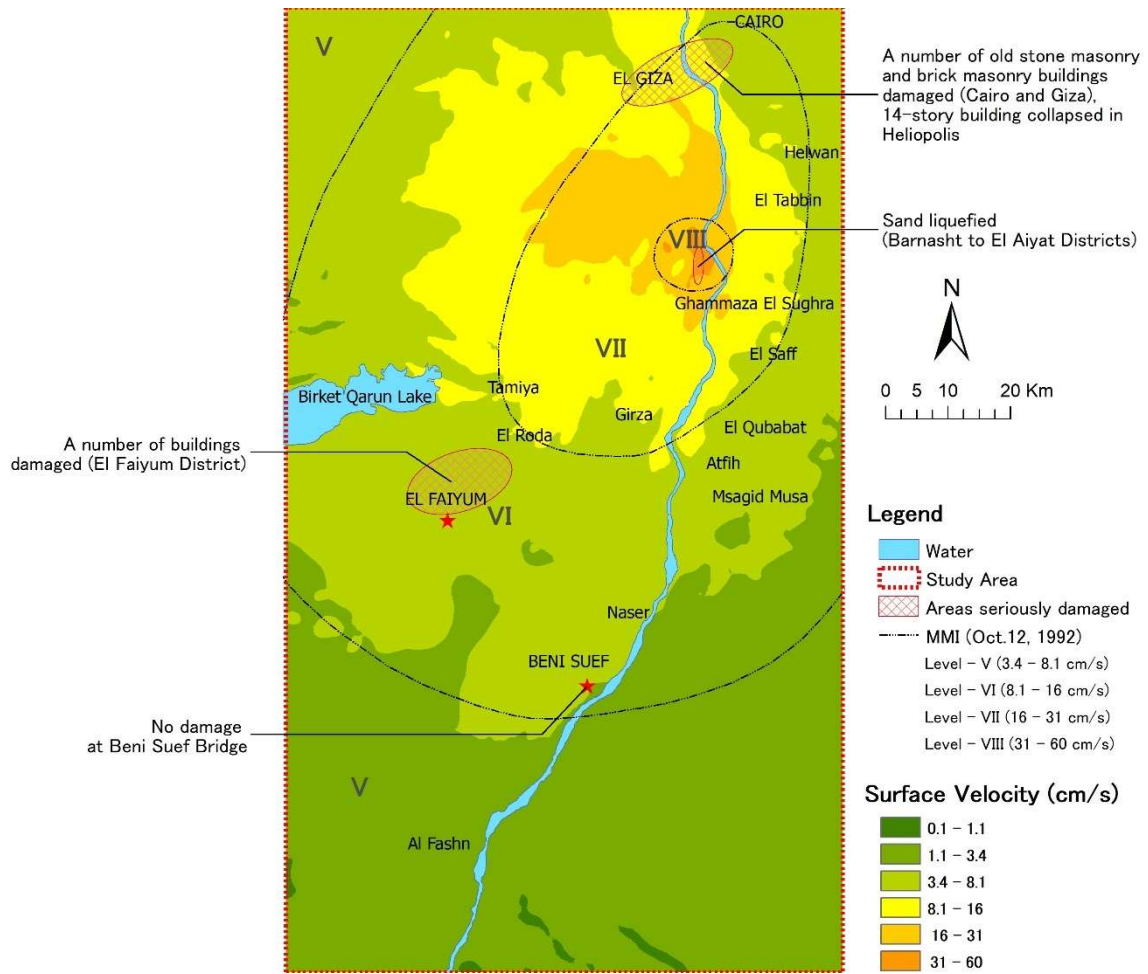


776

777

Fig. 9 Modified Mercalli Intensity (MMI) distribution map of October 12, 1992, Dahshour earthquake (after Thenhaus et al. 1993), and study area (red dotted lines)

778



779

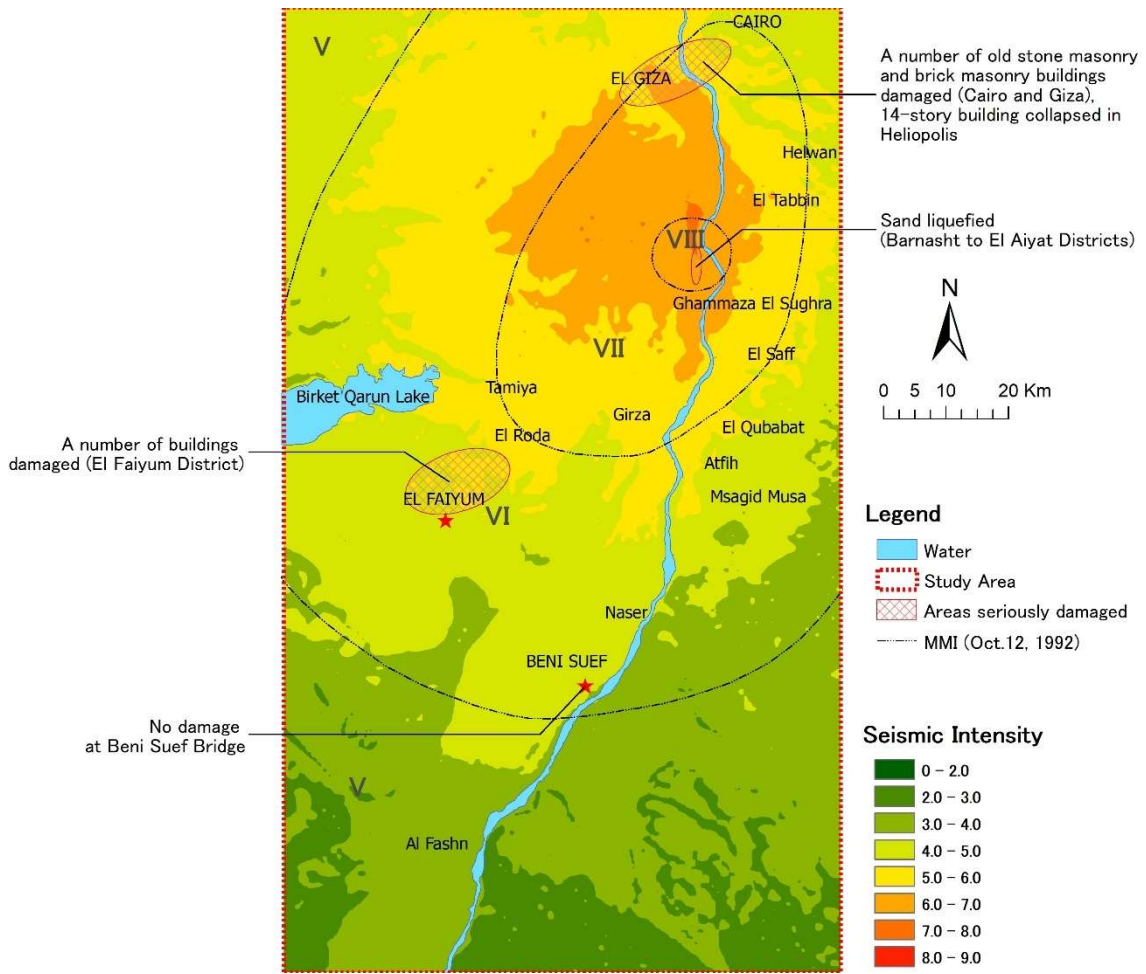
780 **Fig. 10a** Simulation of surface velocity distribution map of October 12, 1992, Dahshour

781 earthquake overlaid with the MMI observation contours and the identified seriously

782

damaged areas

783



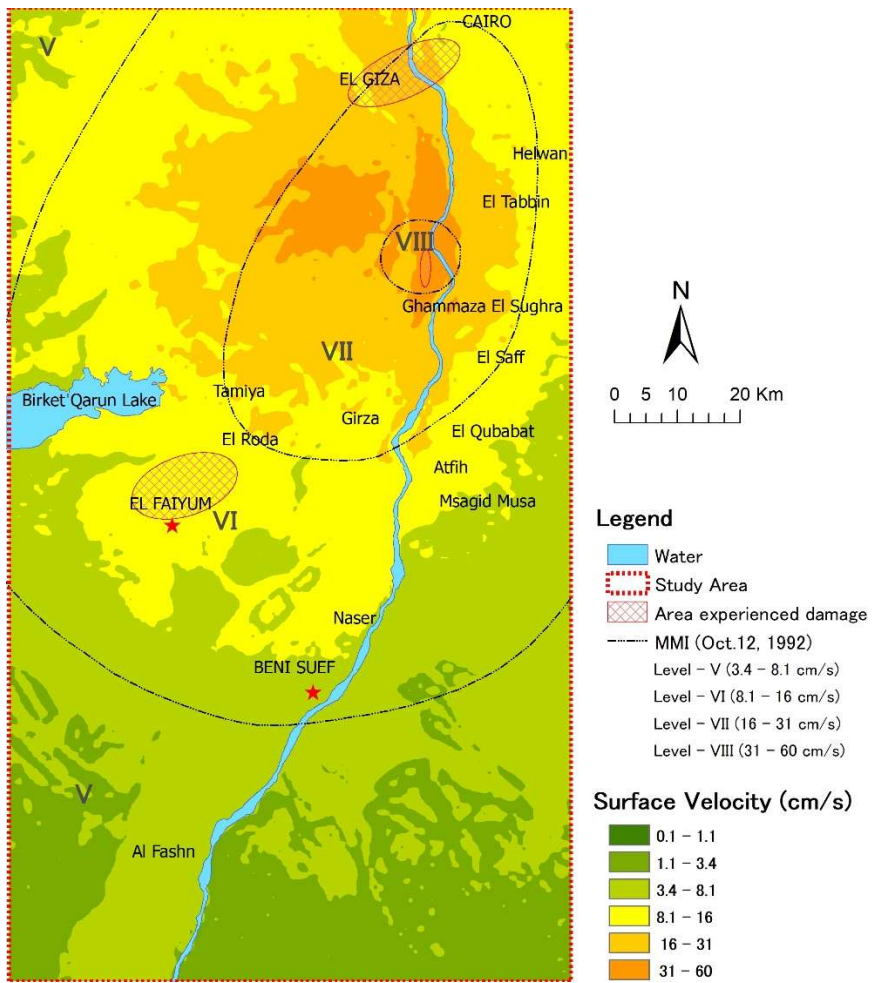
784

785

786

787

Fig. 10b Simulation of seismic intensity distribution map of October 12, 1992, Dahshour earthquake overlaid with the MMI observation contours and the identified seriously damaged areas

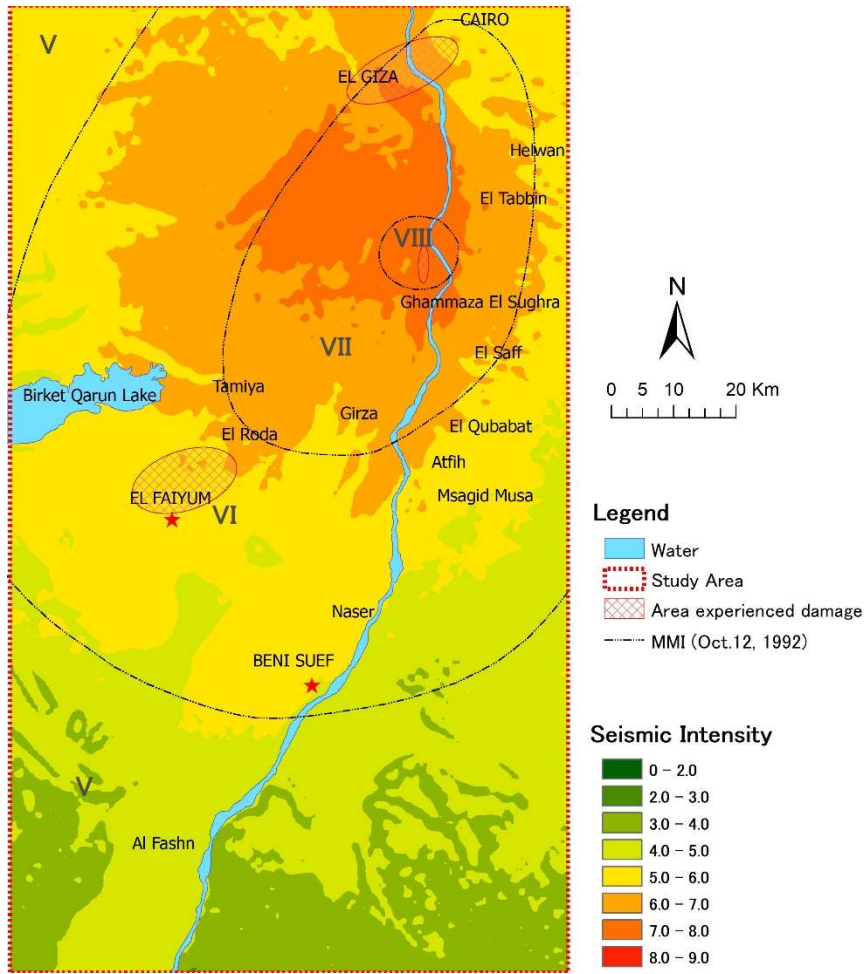


788

789

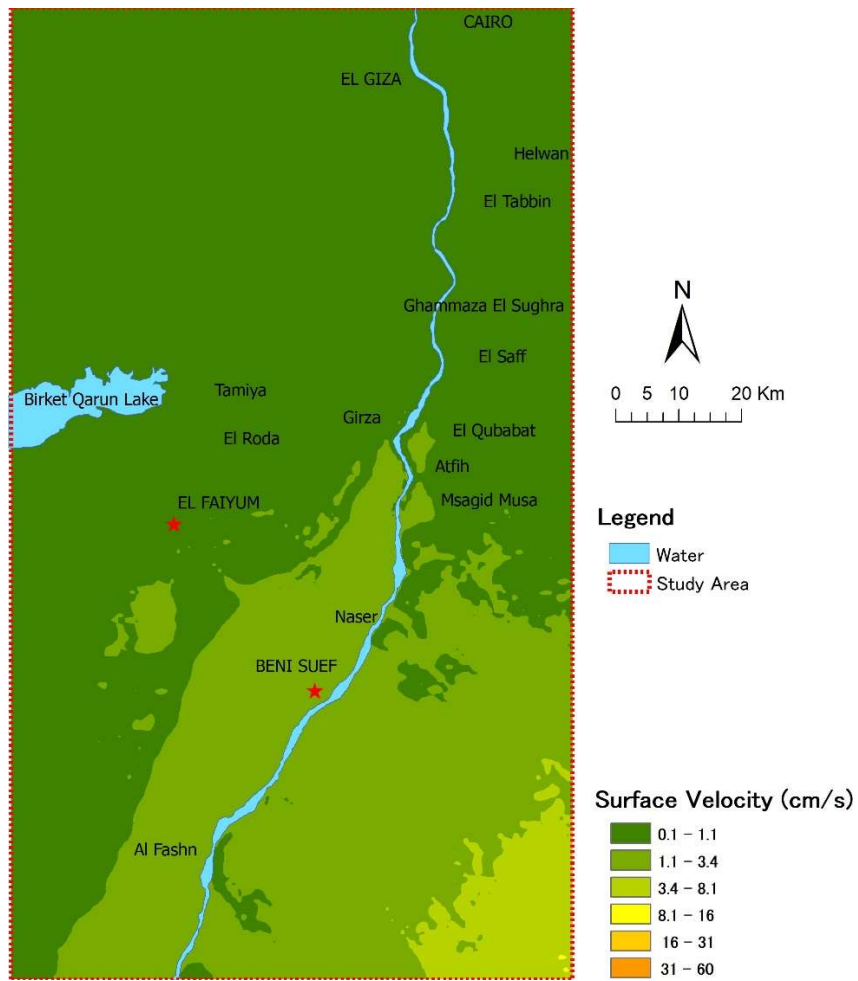
790

Fig. 11a Simulation of surface velocity distribution map of expected 6.5 magnitudes Dahshour earthquake



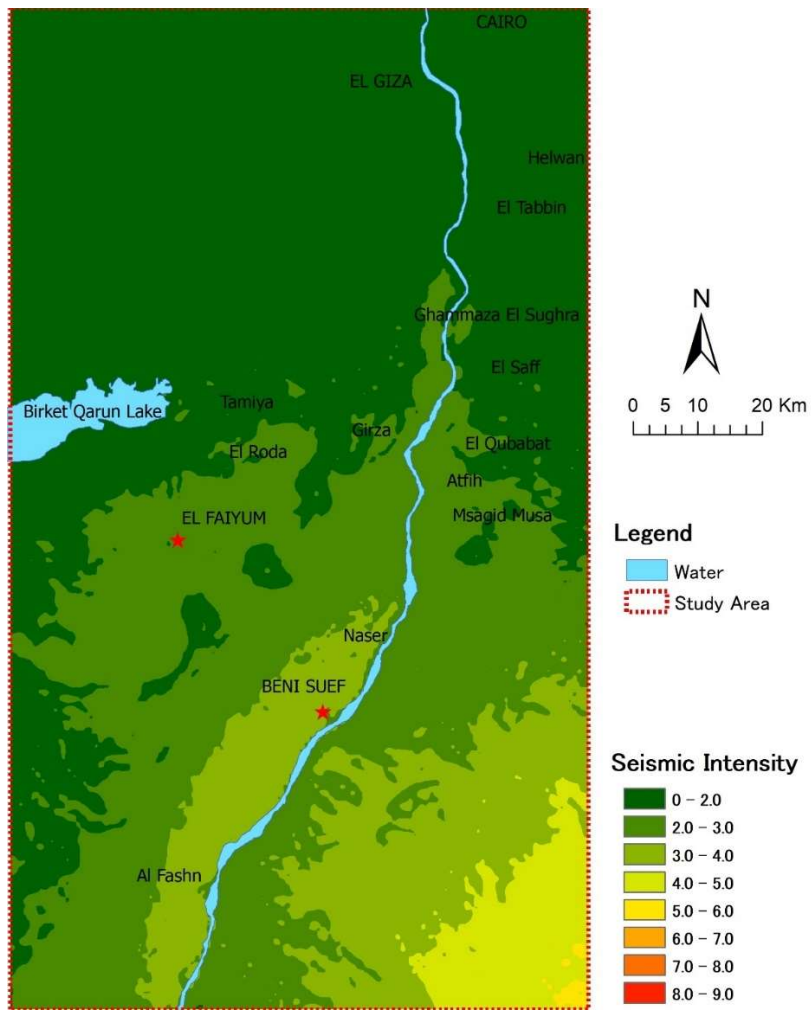
791
 792
 793
 794
 795
 796
 797
 798

Fig. 11b Simulation of seismic intensity distribution map of expected 6.5 magnitudes Dahshour earthquake



799
800
801
802

Fig. 12a Simulation of surface velocity distribution map of October 11, 1999, Beni Suef earthquake



803
 804
 805
 806

Fig. 12b Simulation of seismic intensity distribution map of October 11, 1999, Beni Suf earthquake